Electrical Conductivity of Carbon Nanotubes: Modeling and Characterization

4 authors, including:

Antonio Maffucci
Università degli studi di Cassino e del Lazio Meridionale
157 PUBLICATIONS   **1,318** CITATIONS

Sergey A. Maksimenko
Belarusian State University
290 PUBLICATIONS   **4,307** CITATIONS

Giovanni Miano
University of Naples Federico II
281 PUBLICATIONS   **2,571** CITATIONS

Some of the authors of this publication are also working on these related projects:

Project
Fast Electrothermal Analysis of On-Chip Power Distribution Networks View project

Project
H2020-MSCA-RISE-2016-734164 Graphene 3D "MULTIFUNCTIONAL GRAPHENE-BASED NANOCOMPOSITES WITH ROBUST ELECTROMAGNETIC AND THERMAL PROPERTIES FOR 3D-PRINTING APPLICATION" View project

4. ELECTRICAL CONDUCTIVITY OF CARBON NANOTUBES: MODELING AND CHARACTERIZATION

SHORT TITLE: CNT ELECTRICAL CONDUCTIVITY

ANTONIO MAFFUCCI
Department of Electrical and Information Engineering, University of Cassino and Southern Lazio, via Di Biasio 43, 03043 Cassino, Italy and INFN – LNF, via E. Fermi, 00044 Frascati, Italy

SERGEY A. MAKSIMENKO
Institute for Nuclear Problem, Belarus State University, Bobruiskaya 11, 220030 Minsk, Belarus

GIOVANNI MIANO
Department of Electrical Engineering and Information Technology, University of Naples Federico II, via Claudio 21, 80125, Naples, Italy

GREGORY YA. SLEPYAN
School of Electrical Engineering Tel Aviv University, 6997801, Tel-Aviv, Israel

Abstract.
A short introduction to the electronics properties of carbon nanotubes (CNTs) is given and applied to the analysis of electric conductivity of isolated and bundled CNTs, either single-wall or multi-wall. The model of the electrical conductivity is presented in a wide frequency range, from DC to visible light. In the low frequency range (up to the THz range), only intraband transitions are considered, whereas for higher frequencies also interband transitions are taken into account. The conductivity model us consistent with the classical Drude model and is able to describe novel phenomena associated to the signal propagation along CNTs, such as plasmon resonances of slow surface waves or intershell tunneling effect.

1

4.1 Introduction.

The main reasons why Carbon Nanotubes (CNTs) have been extensively explored as electronic materials reside in their intrinsic advantages for high-performance applications, due to their outstanding properties [1-4].

Indeed, in the last decade several nanoelectronics applications have been suggested for CNTs, such as nano-interconnects, nano-antennas, lumped passives, diodes and transistors, memories, plastic and transparent devices, e.g. [5-15]. Recently, their properties have also suggested their use for the THz technology, e.g., [16].

One of the main reason of this success is to be found in their novel electromagnetic properties, due to many quantum phenomena involved in such 1D nanostructures. In general, they are related to the spatial confinement of the charge carriers motion to sizes comparable with the de Broglie wavelength, what thereby produces a discrete spectrum of energy states in one or several directions. As a result, specific dispersion laws manifest themselves in nanostructures providing their unusual electromagnetic response. This is the reason why, in view of all the above-mentioned potential applications, is it of great interest to fully understand the behavior of such carbon materials.

This Chapter is devoted to modeling the electrical conductivity of CNTs, in view of their above-mentioned potential applications discussed in the other Chapters. A short introduction to the electronics property of CNTs is given in Section 4.2, which allows the further introduction of a conductivity model, given in Section 4.3 for isolated in CNTs and in 4.4 for bundled CNTs. Such a model describes accurately the electrical transport up to the frequency range of some THz, where only intraband transitions are allowed. In this frequency range, novel phenomena may occur, which are of great potential interest for applications, such as plasmon resonance or intershell tunneling: they are discussed in Section 4.3 and 4.4, respectively.

Finally, in Section 4.5 we introduce the possibility of having interband transitions, which allows extending the conductivity model to optical range.

4.2 Band structure of carbon nanotubes and energy subbands

Let us briefly review the band structure of the graphene, whose Bravais lattice is depicted in Figure 1a. The unit cell is spanned by the two basis vectors $\mathbf{a}_1, \mathbf{a}_2$ of length $a_0 = \sqrt{3}b$, being $b = 1.42$ Å the interatomic distance. In the reciprocal k-space depicted in Figure 1b, the graphene is characterized by the unit cell Σ_g, spanned by the two vectors $\mathbf{b}_1, \mathbf{b}_2$ of length $b_0 = 4\pi\sqrt{3}a_0$ [1,3].

The graphene possesses four valence electrons for each carbon atom. Three of these (the so-called *σ-electrons*) form tight bonds with the neighboring atoms in the plane and do not play a part in the conduction phenomenon. The fourth electron (the so-called *π-electron*), instead, may move freely between the positive ions of the lattice.

In the nearest-neighbors tight-binding approximation, the energy dispersion relation of the π-electrons is given by:

$$\mathcal{E}^{(\pm)}(\mathbf{k}) = \pm\gamma\left[1 + 4\cos\left(\frac{\sqrt{3}k_x a_0}{2}\right)\cos\left(\frac{k_y a_0}{2}\right) + 4\cos^2\left(\frac{k_y a_0}{2}\right)\right]^{1/2}, \qquad (1)$$

where $\mathcal{E}^{(\pm)}$ is the energy, the + sign denotes the conduction band, the − sign denotes the valence band and $\gamma = 2.7\text{eV}$ is the carbon-carbon interaction energy. The valence and conduction bands touch themselves at the six vertex of each unit cell, the so-called *Fermi points*. In the neighborhood of each Fermi point the energy dispersion relation may be approximated as

$$\mathrm{E}^{(\pm)} \approx \pm\hbar v_F \left|\mathbf{k} - \mathbf{k}_0\right|, \qquad (2)$$

where $\mathbf{k}_0$ is the wavenumber at a Fermi point, $v_F \approx 0.87 \cdot 10^6$ m/s is the Fermi velocity of the π-electrons, and $\hbar$ is the Planck constant.

In the ground state the valence band of the graphene is completely filled by the π-electrons. In general, at equilibrium the energy distribution function of π-electrons is given by the Dirac-Fermi function:
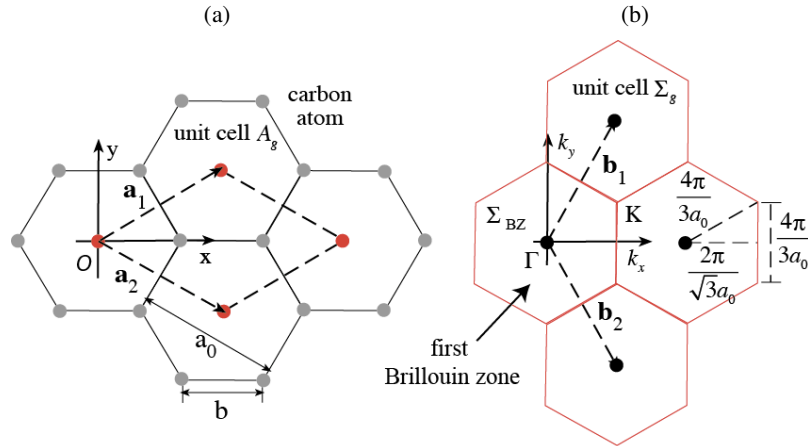

Figure 1. Structure of the graphene. (a) Bravais lattice. (b) Reciprocal lattice.
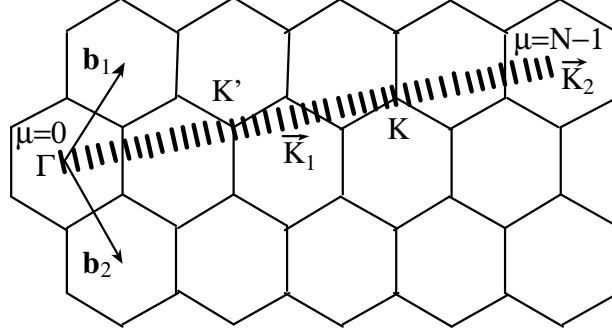
Figure 2. The first Brillouin zone of a CNT is the set of line segments s_μ parallel to $\mathbf{K}_2$. Vectors $\mathbf{K}_1$ and $\mathbf{K}_2$ are reciprocal lattice vectors to $\mathbf{C}$ and $\mathbf{T}$, respectively.

$$F\left[\mathcal{E}^{(\pm)}\right] = \frac{1}{e^{\mathcal{E}^{(\pm)}/k_B T_0} + 1}, \tag{3}$$

where k_B is the Boltzmann constant and T_0 is the absolute temperature.

As known, a carbon nanotube is obtained by rolling up a graphene layer. Its unit cell in the direct space is the cylindrical surface generated by the chiral vector $\mathbf{C} = n\mathbf{a}_1 + m\mathbf{a}_2$ and the translational vector $\mathbf{T} = t_1\mathbf{a}_1 + t_2\mathbf{a}_2$, where n and m are integers, and its circumference is given by $C = a_0\sqrt{n^2 + nm + m^2}$. The first Brillouin zone of a SWCNT is the set of N parallel segments $s_\mu, \mu = 0,..N-1$, of the graphene reciprocal lattice, depicted in Fig. 2. Each segment has a length of $T = |\mathbf{T}|$, and is orthogonal to $\mathbf{K}_1$ and parallel to $\mathbf{K}_2$, being such vectors:

$$\mathbf{K}_1 = \left(-t_2\mathbf{b}_1 + t_1\mathbf{b}_2\right)/N, \quad \mathbf{K}_2 = \left(m\mathbf{b}_1 + n\mathbf{b}_2\right)/N \tag{4}$$

The longitudinal wave vector k is almost continuous because the length of the CNT is assumed to be very large compared with the length of the unit cell.

The transverse wave vector $k_\perp$ is quantized: it takes only the discrete values $\mu\Delta k_\perp$ with $\mu = 0,1,...,N-1$. In the zone-folding approximation the dispersion relation for the SWCNT is given by [1,17]:

$$\mathcal{E}_\mu^{(\pm)}(k) = \mathcal{E}^{(\pm)}\left(k\frac{\mathbf{K}_1}{|\mathbf{K}_2|} + \mu\mathbf{K}_1\right) \text{ for } -\frac{\pi}{T} < k < \frac{\pi}{T} \text{ and } \mu = 0,1,...N-1, \tag{5}$$

where $\mathcal{E}^{(\pm)}$ is given by (1).

Nanotubes are denoted as *zig-zag* if $n = 0$ or $m = 0$, *armchair* if $n = m$ and *chiral* in all other cases. The general condition for a CNT to be metallic is $|n - m| = 3q$, where $q = 0,1,2,..$, therefore, armchair CNTs are always metallic, whereas zig-zag CNTs are metallic only if $m = 3q$. Figure 3 shows the typical band structures for a metallic and a semiconducting CNT.
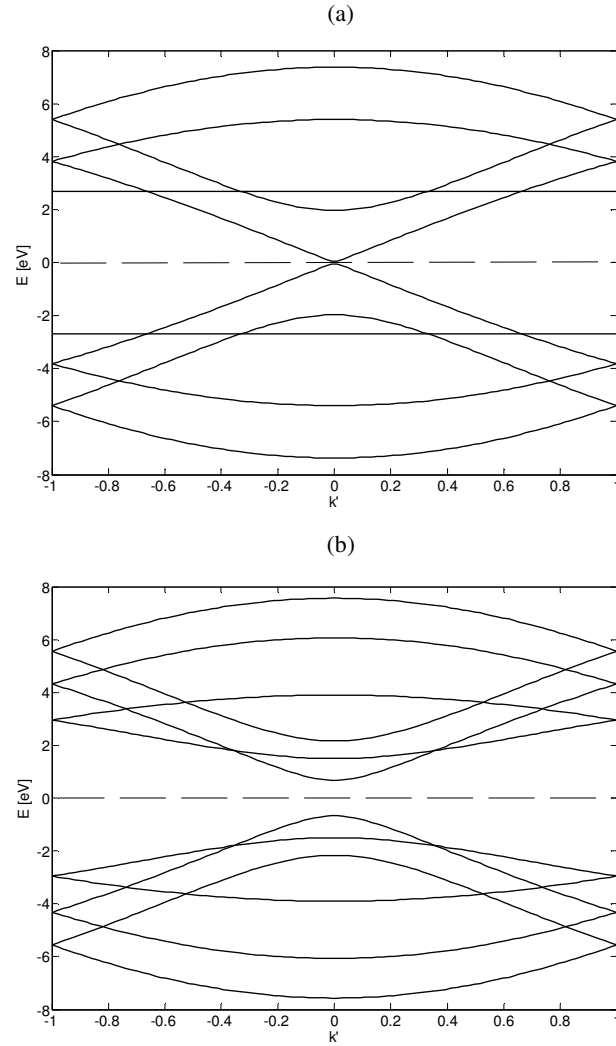
(a)

(b)

Figure 3. Typical band structure for a metallic (a) and a semiconducting (b) CNT.

4.3 Electrical conductivity of isolated CNTs, from DC to THz range

4.3.1 Transport equation

In view of modeling the CNT conductivity, we must investigate the interaction of π-electrons with electromagnetic field. Within the quasi-classical approximation, these electrons are modeled as a 1D electron Fermi-gas which is in the equilibrium state, in the absence of electromagnetic field. Under the action of the field, the π-electrons execute intraband motion, with negligible interband transitions. This limits the mode to frequency range up to Terahertz (THz) or Far Infra-Red (FIR) ranges.

Under the above conditions, electron gas in CNT is characterized by a distribution function of π-electrons, whose intraband motion is described by the Boltzmann equation for the distribution function. Elimination of interband transitions does not mean overall neglecting quantum effects, what is outlined by the adjective "quasi-classical". Indeed, electrons in CNT are not classical particles; their quantum nature manifests itself even in intraband motion. First of all, π-electrons are *fermions* and, therefore, their quantum nature establishes their equilibrium distribution as the Fermi distribution (3). Furthermore, π-electrons are not free electrons: their quantum-mechanical interaction with the CNT crystalline lattice is responsible for their particular dispersion law.

Assuming a transversally symmetric surface wave interacting with the π-electrons, the distribution function $f(\mathbf{p}, z, t)$ satisfies the following Boltzmann kinetic equation [18]:

$$\frac{\partial f}{\partial t} + v_z \frac{\partial f}{\partial z} + eE_z \frac{\partial f}{\partial p_z} = \nu[F(\mathbf{p}) - f],$$
(6)

where e is the electron charge, $\mathbf{p}$ is the two-dimensional quasi-momentum, tangential to the CNT surface, p_z is the projection of $\mathbf{p}$ on the CNT axis z, $v_z = d\mathcal{E}/dp_z$ is the velocity, and $F(.)$ is the Fermi distribution (3). The relaxation term (collision integral) in the r.h.s. of (6) is assumed to be momentum-independent [19], thus described by the *collision frequency* ν, *i.e.*, the reciprocal of the time between two collisions $\nu = v_z/\lambda$, being λ the electron mean free path.

The solution of (6) is can be linearized in the weak-field regime. Assuming $E_z = \text{Re}[E_z^0 \exp(i(\omega t - kz))]$, putting $f = F + \text{Re}[\delta f \exp(i(\omega t - kz))]$, and taking only the linear terms, we obtain:

$$\delta f = -i \frac{\partial F}{\partial p_z} \frac{eE_z^0}{\omega - kv_z + i\nu}. \tag{7}$$

The axial surface current density $J_z = \mathrm{Re}\left[J_z^0 \exp(i(\omega t - kz)) \right]$ is then given by:

$$J_z^0(\omega,k) = \tilde{\sigma}_{zz}(\omega,k)E_z^0(\omega,k), \tag{8}$$

where the axial conductivity in the wavenumber domain is expressed as:

$$\tilde{\sigma}_{zz}(\omega,k) = -i\frac{2e^2}{(2\pi\hbar)^2} \iint_{1stBZ} \frac{\partial F}{\partial p_z} \frac{v_z d^2\mathbf{p}}{\omega - kv_z + i\nu}; \tag{9}$$

here the integral spans over the first Brillouin zone (1stBZ).

To compute (9) we should refer to a given electron dispersion relation $\mathcal{E}(\mathbf{p})$. Assuming zig-zag CNTs, (9) would become:

$$\tilde{\sigma}_{zz}(\omega) = -2ie^2 n_0 \frac{1}{(\omega + i\nu)F_0} \iint_{1stBZ} v_z^2(\mathbf{p}) \frac{\partial F}{\partial \mathcal{E}} d^2\mathbf{p}, \tag{10}$$

where

$$F_0 = \iint_{1stBZ} F(\mathbf{p})d^2\mathbf{p}, \tag{11}$$

and n_0 is the surface density of conduction-band electrons in graphene. Note that, for infinite CNT radius, the dynamic axial conductivity of a CNT becomes locally equivalent to the dynamic conductivity of semi-metallic graphene:

$$\sigma_\infty = i\frac{2\ln 2}{\pi\hbar^2} \frac{e^2 k_B T_0}{\omega + i\nu}. \tag{12}$$

The numerically evaluated axial conductivity (10) is reported in Fig.4 as a function of the chiral index m (with $n = 0$), assuming $\nu = 0.33 \cdot 10^{12}$ s^{-1}, and $T_0 = 264$ K. Since the radius of a zigzag CNT is given by $R_c = \sqrt{3}mb/2\pi$ [1], Fig.4 actually shows the dependence of $\tilde{\sigma}_{zz}$ on the cross-sectional radius. As R_c increases ($m > 300$), $\tilde{\sigma}_{zz}$ approaches σ_∞. The results show a sharp increase corresponding to $m = 3q$ (where q is an integer), i.e. to metallic condition for zig-zag CNTs. For the metallic case, it results:

$$\tilde{\sigma}_{zz} = i\frac{2\sqrt{3}}{m\pi\hbar^2} \frac{e^2 \gamma}{\omega + i\nu}. \tag{13}$$
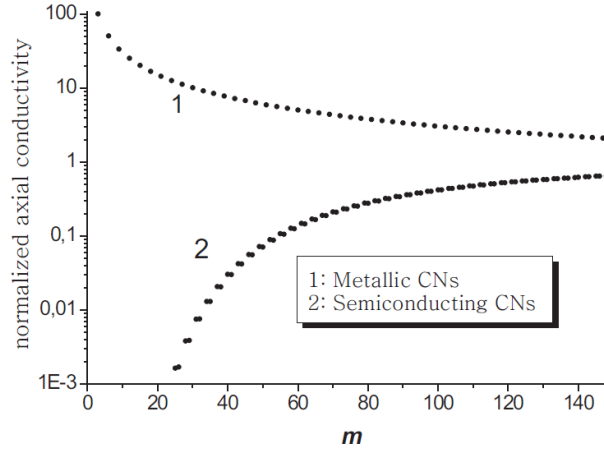
Figure 4. Normalized axial conductivity for zig-zag CNT, vs chiral number *m* (*i.e.*, vs CNT radius). The conductivity is normalized to that of the graphene (12) [18].
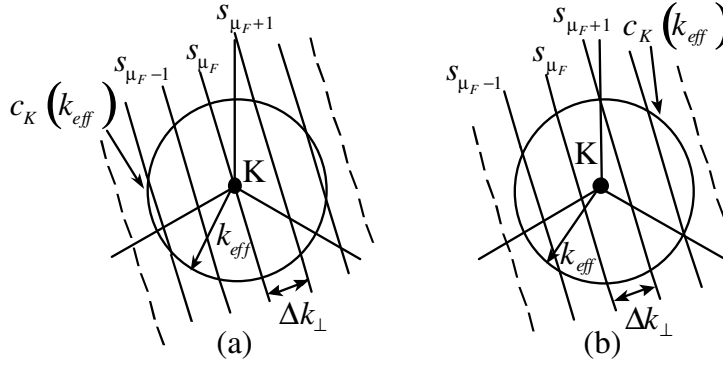

Figure 5. Segments s_μ around the Fermi point *K* for: (a) a metallic and (b) a semiconducting CNT. Only the full line segments contribute effectively to the CNT axial conductivity.

To understand such a behavior, let us note that only energy subbands that pass through or are close to the CNT Fermi level contribute significantly to the CNT axial conductivity. In the Brillouin zones in Fig.2, there are only two inequivalent graphene Fermi points contained by or are nearest to some segments s_μ, indicated with *K* and *K'*. Figure 5 shows the segments around *K*: for metallic CNTs, there is one segment passing through *K*, resulting in the drastic growth of the numerical value of the integral in (10). For semiconducting CNTs, no segment passes through *K*. Note that the segments that contribute significantly to $\tilde{\sigma}_{zz}$ are those falling in a circle c_k of radius $k_{eff} \approx 5 k_B T_0 / \hbar v_F$: this provides a criterion to evaluate the limited number of subbands which significantly contribute to the conduction. Note that this also implies the dependence of $\tilde{\sigma}_{zz}$ on temperature.

The case of armchair CNTs may be treated with the same approach, using the corresponding dispersion relation $\mathcal{E}(\mathbf{p})$ to solve (10). The numerically evaluated conductivity $\tilde{\sigma}_{zz}$ is shown in Fig.6, vs the chiral number m. For small CNT radius ($m < 50$), $\tilde{\sigma}_{zz}$ may be approximated as in (13), divided by $\sqrt{3}$. Unlike for zigzag CNTs, for armchair CNTs the dependence is monotonic. Physically, this follows from the fact that armchair CNTs are conductors for any m. Again, for $m \rightarrow \infty$ (i.e. $R_c \rightarrow \infty$), it is $\tilde{\sigma}_{zz} \rightarrow \sigma_\infty$.

Finally, in the general case of chiral CNTs ($n \neq m > 0$), an applied axial electric field would induce the current to flow along a helical line. Therefore, besides the axial conductivity, we should also consider an azimuthal component. However, in the linear regime such a component was shown to be negligible [20-22]. For a metallic chiral CNT of radius r_c, $\tilde{\sigma}_{zz}$ may be approximated as:

$$\tilde{\sigma}_{zz} = i \frac{3e^2 b\gamma}{\pi^2 \hbar^2 r_c} \frac{1}{\omega + i\nu}. \tag{14}$$
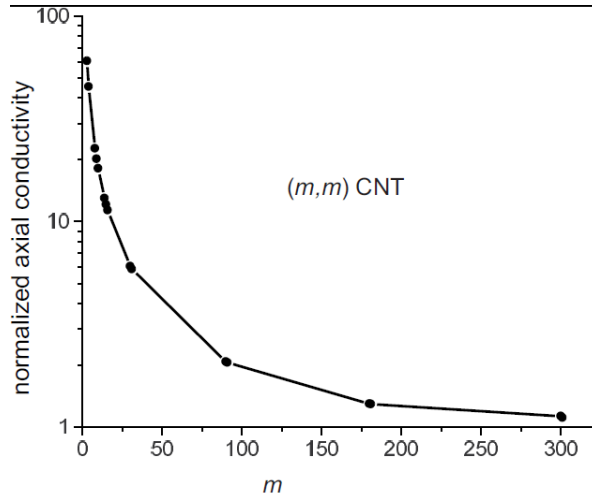

Figure 6. Normalized axial conductivity for armchair CNT, vs chiral number m (*i.e.*, vs CNT radius). The conductivity is normalized to that of the graphene (12) [18]

4.3.2 Equivalent parameters for an isolated CNT

In the frequency domain, taking into account Boltzmann equation (6) and constitutive relation (8), the relation between current, charge and field can be written as follows:

$$\left(\frac{i\omega}{\nu}+1\right)J_z + \frac{v_F^2}{\nu}\frac{\partial\rho_s}{\partial z} = \sigma_c E_z, \tag{15}$$

where $\rho_s(z,\omega)$ is the surface charge density, and σ_c is the long wavelength static limit for the axial conductivity:

$$\sigma_c = \frac{v_F}{\pi r_c \nu R_0} M . \tag{16}$$

In (16) we introduced the *quantum resistance* $R_0 = \pi\hbar/e^2 \cong 12.9\,\text{k}\Omega$, and the *equivalent number of conducting channels M*. This latter parameter takes into account the contribution to the conductivity given by those segments s_μ passing through the two circles in Fig.5, and may be evaluated by [17, 23]:

$$M = \frac{2\hbar}{v_F}\sum_{\mu=0}^{N-1}\int_0^{\pi/T} v_F^2\left(\frac{dF}{dE_\mu^+}\right)dk. \tag{17}$$

Let us now further investigate the physical meaning of the coefficients of the linear transport equation (15). In the considered frequency range (up to THz), at the generic abscissa z, the current intensity and charge densities are almost uniform over the CNT circumference C, therefore we can assume:

$$i(z,t) \approx 2\pi r_c j_z(z,t), \quad q(z,t) \approx 2\pi r_c \rho_s(z,t). \tag{18}$$

By using (18), transport equation (15) may be rewritten in time domain as:

$$L_k\frac{di(z,t)}{dt} + Ri(z,t) + \frac{1}{C_q}\frac{\partial q(z,t)}{\partial z} = E_z(z,t), \tag{19}$$

where the electrical parameters L_k, R, and C_q have the dimensions of per-unit-length (p.u.l.) inductance, resistance, and capacitance, respectively, given by:

$$L_k = \frac{R_0}{2v_F M}, \quad R = \nu L_k, \quad C_q = \frac{v_F^2}{L_k}. \tag{20}$$

These parameters are associated to three major phenomena exhibited by the CNT electrodynamics: L_k is also known as the *kinetic inductance* of the CNT,

which adds to the classical magnetic inductance. Usually, L_k is 3-4 orders of magnitude greater than the magnetic one. From a physical point of view, L_k is associated to the kinetic energy of the π-electrons. The parameter C_q is, instead, the *quantum capacitance* of the CNT, associated from a physical point of view to the internal energy of the π-electrons at the ground state. Finally, the resistance R takes into account all the scattering mechanisms associated to the electron transport along the CNT lattice, since $\nu = v_F / \lambda$. An approximation for the mean free path λ is given by Mathiessen rule [24]:

$$\lambda^{-1} = \lambda_{AC}^{-1} + \lambda_{OP,ems}^{-1} + \lambda_{OP,abs}^{-1}, \tag{21}$$

which includes elastic electron scattering with AC phonons (λ_{AC}), inelastic electron scattering by optical phonons emission $(\lambda_{OP,ems})$ and absorption $(\lambda_{OP,abs})$. Experimental evidences and theoretical models indicate that λ varies with CNT chirality, diameter and temperature (*e.g.,* [25]). All these parameters are strongly dependent on the number of conducting channels M (17), which in turn depends on CNT chirality radius and temperature. In fact, as the CNT radius increases, $\Delta k_\perp = 1/r_c$ decreases. In addition, as the absolute temperature T_0 increases, the radius k_{eff} increases too. As a consequence, M is an increasing function of both CNT radius and temperature, as shown in Fig.7, for metallic and semiconducting CNTs.
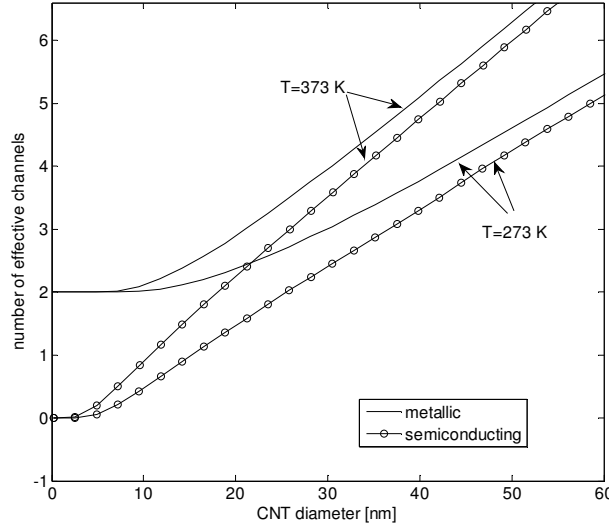

Figure 7. Equivalent number of conducting channels vs CNT diameter, at *T*=273 K and *T*=373 K.

For SWCNTs, with radius of some nm, it is $M \approx 2$ ($M \approx 0$) for the metallic (semiconducting) case, and thus only the metallic SWCNTs contribute to the conduction. Instead, for MWCNT shells, whose radius is typically of the order of tens of nm, the contributions of semiconducting CNTs is not negligible. The following piecewise linear fitting may be adopted for the generic CNT shell of diameter D, whose parameters are reported in Table 1 [23].

$$M_{shell}(D;T) \cong \begin{cases} M_0 & \text{for } D < D_0(T) = d_0/T \\ a_1 DT + a_2 & \text{for } D > D_0(T) = d_0/T \end{cases}. \quad (22)$$

For small diameters metallic CNTs it is $M \approx 2$, hence parameters (20) become:

$$L_k = \frac{R_0}{4v_F} \approx 3.6\,\text{nH/}\mu\text{m}, \quad C_q = \frac{R_0 v_F}{4} \approx 350\,\text{aF/}\mu\text{m}. \quad (23)$$

As the CNT diameter increases, the kinetic inductance increases and the quantum capacitance decreases, as shown in Fig.8.

TABLE I: FITTING VALUES FOR FORMULA (22)

	SWCNT (metallic)	SWCNT (semicond.)	MWCNT shell
M_0	2	0	2/3
a_1 [nm^{-1}K^{-1}]	$3.26 \cdot 10^{-4}$	$3.26 \cdot 10^{-4}$	$3.26 \cdot 10^{-4}$
a_2	0.15	-0.20	-0.08
d_0 [nm·K]	5600	600	1900

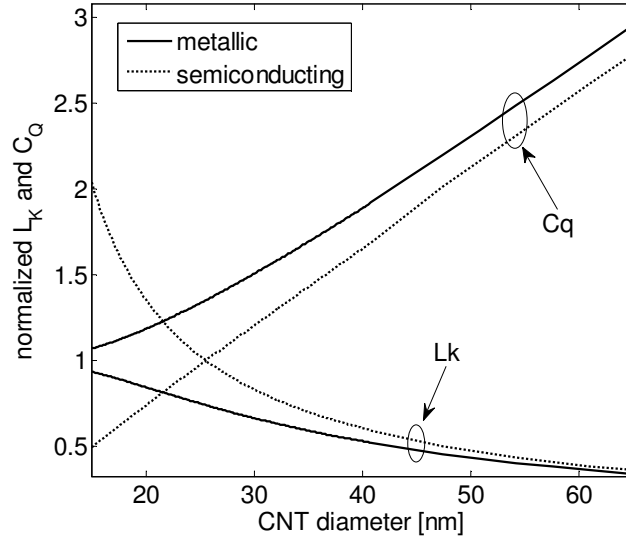*Figure 8.* Kinetic inductance and quantum capacitance, normalized to the values in (23) versus the CNT diameter, for $T = 273$K: metallic (solid lines) and semiconducting case (dotted lines).

4.3.3 Plasmon resonances in CNTs

According to the results presented in previous sections, the nanotubes allow the propagation of slowly decaying surface waves (plasmons), with almost frequency-independent wavenumber and the phase velocity much smaller than the speed of light in vacuum. These properties make CNTs excellent candidates for the design of nanoantennas [5-7]. To understand this result, we can analyze the simple case of an isolated CNT, whose circuit parameters were derived in 4.3.2. In the considered frequency range, the propagation may be modeled by a simple RLC lossy transmission line (TL) model [14], whose parameters are approximately given (assuming $L_k \gg L_M$) by: R, $L \approx L_k$, and $C \approx C_E$, being C_E the electrostatic capacitance. A consequence of the huge value of the kinetic inductance is a low phase velocity, typically, $c_{CNT} \approx 10^{-2}c$, where c is the value for an ideally-scaled copper interconnect of same dimensions. The plasmon resonances are then obtained by imposing the classical resonance condition along a TL, that is $\beta l = n\pi/2$, with $n = 1,2,3$.

The phenomena of plasmon resonance may be also observed in higher frequency ranges, for instance in the Far Infrared (FIR) range. In order to investigate such a range, a rigorous evaluation of the CNT conductivity is needed, taking into account both intraband and interband transitions. This can be done, for instance, by means of the method of Effective Boundary Conditions (EBC), as shown in [18]. The general model for conductivity in such ranges will be discussed in Section 4.5 and will lead to a conductivity behavior like that reported in Fig.9, referring to a 200 nm-long SWCNT.
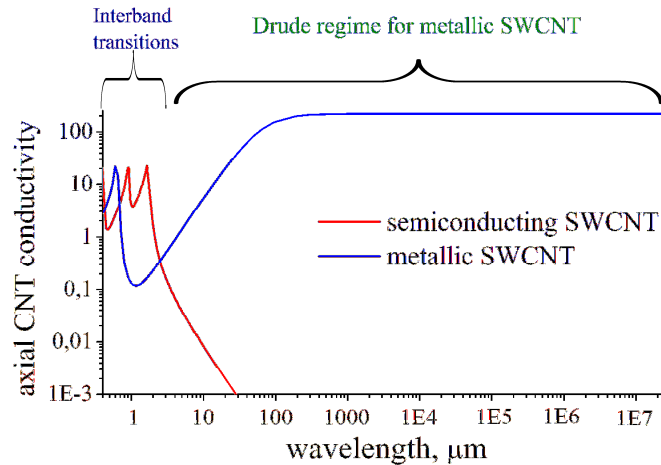

Figure 9. Axial CNT conductivity vs wavelength for a SWCNT of length 200 nm.

Three regions may be easily distinguished. In the low frequency range ($\lambda > 300\,\mu m \rightarrow f < 1\text{THz}$) the conductivity attains its quasi-static value, and metallic CNTs exhibits a classical Drude behavior. In the high frequency range ($\lambda < 3\,\mu m \rightarrow f > 100\text{THz}$), the conductivity is dominated by the interband transitions (see Sect. 4.5 for details).

The intermediate region is the most interesting for THz applications: in such a region, the dispersion relation for the propagating surface wave reads [18]:

$$\frac{\kappa^2}{k^2} K_q(\kappa r_c) I_q(\kappa r_c) = \frac{ic}{4\pi r_c \sigma_{zz}}\left[1 - (\kappa^2 + k^2)\right], \qquad (24)$$

where $K_q(.), I_q(.)$ are the modified Bessel functions, c is the speed of light in vacuum, $\kappa^2 = h^2 + k^2$ and h is the surface wave wavenumber. Compared to classical dispersion laws in microwave range, the presence of the CNT conductivity σ_{zz} in (24) is responsible for the unusual electromagnetic response of these nanostructures. In fact, Fig.10 shows the wavenumber $\beta = k/h$, computed from (24) for an axially symmetric plasmon along a metallic zig-zag SWCNT of length 0.6 µm. In the THz and IR ranges, the surface waves are associated to an almost frequency-independent wavenumber β, with a phase velocity given by $v_{ph} \approx 0.02c$. The positions of the plasmon resonances satisfies the above-mentioned condition: the first antenna resonance at n=1 is also known as the localized plasmon resonance [26].
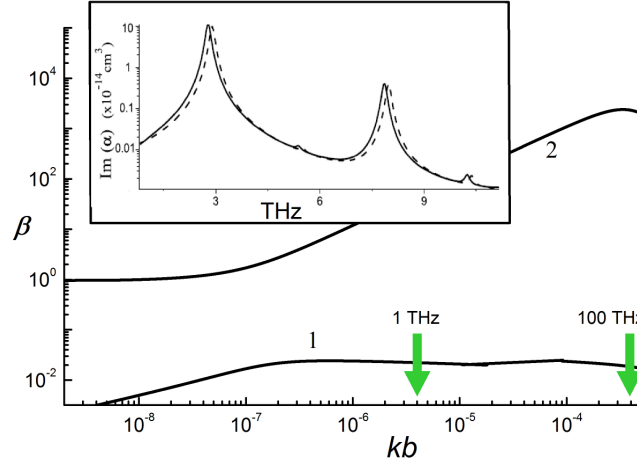

Figure 10. The slow-wave coefficient β in a (9,0) metallic zigzag SWCNT for relaxation time τ=3ps and T=295 K [18], *b*=1.42 Å is the C-C bond length. 1: Re(β); 2: Re(β)/Im(β). Inset: antenna resonances in polarizability of a 0.6 µm length (18,0) zigzag SWCNT [7].

The first experimental evidence of plasmon nature of the THz peak in SWCNTs was given in [27], where a FIR peak was found to shift to higher frequencies after decreasing the CNT length. A broad peak in the THz and FIR ranges was observed in the conductivity spectrum of composite materials containing SWCNTs [28-35]. Two hypotheses have been advanced to explain such a peak, as an effect of the finite CNT radius or of the finite CNT length. The plasmon nature of such resonances is evident from Fig.11, which shows the results of an experiment carried out on a thin film containing SWCNTs with controlled lengths, [36]. The length distributions of four sets are shown in Fig.11 (a)-(d), whereas Fig.11(e) shows a resonance peak in the optical density spectra which shifts to lower values for longer CNTs. The nature of plasmon excitation in SWCNTs was independently proved by alternative experiment [37], which is based on the idea that only metallic nanotubes contribute into THz peak if its nature is related to antenna (plasmon) resonance, while substitutional doping of CNTs increases "metallicity" of nanotubes. Theoretical model and experimental demonstration of the increase were reported in [38] and [39], respectively. The plasmon nature of TCP was also reported in [40], on the basis of experiments analogous to that carried out in [27].
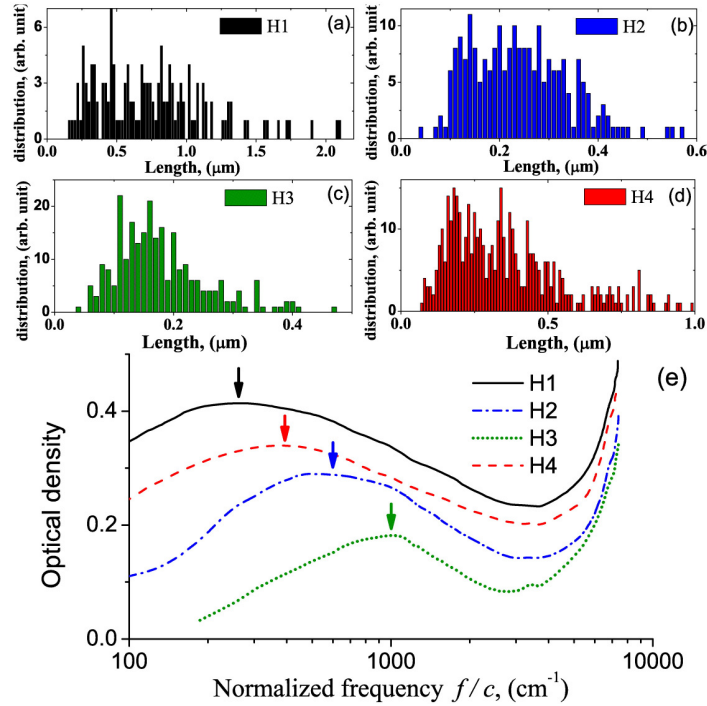

Figure 11. Distributions of CNT lengths in the thin film (a)-(d); optical density spectra for the four sets showing the THz peaks (see arrows) [27].

4.4 Equivalent resistivity for a CNT bundle from DC to THz

4.4.1 A bundle of CNTs without intershell coupling

As pointed out in this Book, CNTs are proposed as emerging research material [41] for interconnects and packages, because of their unique electrical, mechanical and thermal properties. CNT interconnects are expected to meet many of the new requirements for bonding, molding compound, underfill, thermal interface, die attach. The electrical performances of CNT interconnects are strongly influenced by the kinetic and quantum phenomena affecting their electrodynamics, and by the presence of a huge contact resistance at the metal/CNT contacts.

The technological solution adopted so far is the use of dense bundles of either SWCNTs or MWCNTs where each individual tube carries the same current, so that the equivalent resistance is strongly reduced by the parallel, like in the schemes reported in Fig.12 for vertical (vias) or in Fig.13 for horizontal interconnects.

In order to derive an equivalent resistivity of these interconnects, let us consider a bundle of length l, composed of N_b CNTs, fed in parallel.
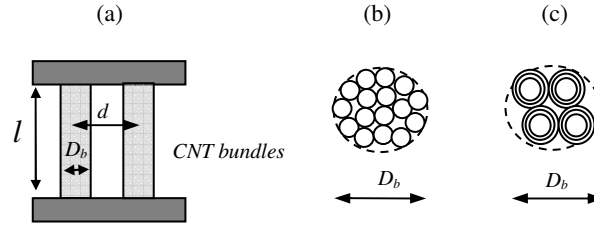

Figure 12. CNT vertical interconnects (vias): (a) geometry; (b) cross section of a SWCNT via; (c) cross section of a MWCNT via.
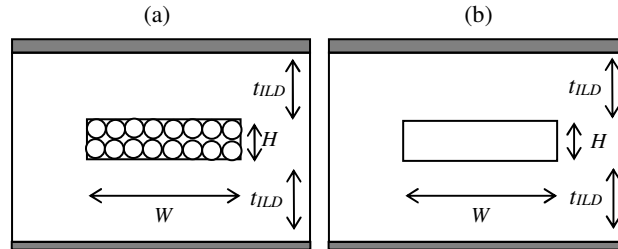

Figure 13. Horizontal interconnect made by: (a) SWCNTs bundle; (b) MWCNTs bundle.

We indicate, respectively, with I_n, V_n, and E_n, the current intensity, the voltage between the ends and the longitudinal component of the total electric field at the surface of the n-th CNT shell with the reference directions for the current intensity and the voltage chosen according to the normal convention. Using (19), the equations governing the transport of the π-electrons may be expressed in matrix form as follows:

$$(i\omega\overleftrightarrow{\mathbf{L}}_k + \overleftrightarrow{\mathbf{R}})\mathbf{I} = l\mathbf{E}, \qquad (25)$$

where $\mathbf{I}$ and $\mathbf{E}$ are column vectors (N_b x 1), of components I_k and E_k, and $\overleftrightarrow{\mathbf{L}}_k$ and $\overleftrightarrow{\mathbf{R}}$ are diagonal matrices whose m-th elements are given by the kinetic inductance and the resistance of each CNT (here and hereafter the symbol $\leftrightarrow$ denotes matrices). For SWCNTs bundle, it means:

$$(R)_{m,m} = \frac{R_0 l}{2M_m \lambda_m}, \quad \left(L_k\right)_{m,m} = \frac{R_0 l}{2M_m v_F}, \qquad (26)$$

where M_m and λ_m are the number of channels and mean-free path of the m-th CNT. In case of MWCNT bundles, each of them containing N_S shells, the above parameters are expressed by:

$$\left(L_k\right)_{m,m} = l\left[\sum_{n=1}^{N_S} \frac{2v_F M_n}{R_0}\right]^{-1}, \quad (R)_{m,m} = l\left[\sum_{n=1}^{N_S} \frac{2M_n \lambda_n}{R_0}\right]^{-1}.$$

In the magneto-quasi-stationary limit we have:

$$i\omega\overleftrightarrow{\mathbf{L}}_m\mathbf{I} = \mathbf{V} - l\mathbf{E}, \qquad (27)$$

where $\overleftrightarrow{\mathbf{L}}_m$ is the classical magnetic inductance matrix of the bundle. By combining (26) and (27) we obtain:

$$(i\omega\overleftrightarrow{\mathbf{L}} + \overleftrightarrow{\mathbf{R}})\mathbf{I} = \mathbf{V}, \qquad (28)$$

where the total inductance is given by $\overleftrightarrow{\mathbf{L}} = \overleftrightarrow{\mathbf{L}}_m + \overleftrightarrow{\mathbf{L}}_k$.

Since all the CNT in the bundle are electrically in parallel it results $V_n = V_b$ where V_b is the voltage drop along the bundle. By solving system (28) with the constraint $V_n = V_b$, for $n = 1,2...N_b$, we obtain the relation between the total current, $I_b = \sum_{n=1}^{N_b} I_n$, and the bundle voltage, expressed as:

$$V_b = Z_b I_b = (\rho_b' + i\rho_b'')\frac{l}{S_b}I_b, \qquad (29)$$

where S_b is the bundle section and $\rho_b = \rho_b' + i\rho_b''$ may be regarded as the *bundle equivalent resistivity*. Assuming that all CNTs in the bundle are equal and that the kinetic inductance dominates over the magnetic one, as usually it is, the equivalent resistivity may be given the form [12]:

$$\rho_b' + i\rho_b'' = \rho_0(1 + i\omega\tau), \tag{30}$$

where the value ρ_0 and the relaxation time τ are given by:

$$\rho_0 = \frac{R_{CNT}S_b}{F_M N_b l}, \quad \tau = \frac{\lambda}{v_F}, \tag{31}$$

where $R_{CNT} = (R)_{m,m}$ is the resistance of the single CNT and F_M is the fraction of metallic CNTs in the bundle. Note that it is usually $F_M = 1/3$ ($F_M = 1$) for SWCNTs (MWCNTs). If we neglect the influence of the terminal contact CNT/metal, then $R_{CNT} = (R)_{m,m}$, but in realistic case we must take into account the effect of contacts, that can be modeled by adding a lumped term [14]:

$$R_{CNT} = (R)_{m,m} + \frac{R_0 + R_p}{M}, \tag{32}$$

where R_p is a parasitic term which goes to zero for ideal CNT/metal contact.

In DC or low-frequency conditions, the equivalent resistivity tends to the real value ρ_0. In the following we evaluate the equivalent resistivity at room temperature for several types of CNT interconnects using the geometries in Fig.9 and Fig.10, and considering two nanoscale technology nodes of integrated circuits: 22 nm and 14 nm. Their geometrical values, taken from the International Technology Roadmap of Semiconductors [41], are reported in Table II. We compare the obtained results with the values of the resistivity of the corresponding copper interconnects, reported in Table III, which are reported in [41] and take into account the resistivity increase with shrinking dimensions, due to electromigration, grain and boundary scattering [42]

For all the CNT realizations, we assume a metallic fraction of 1/3, a parasitic resistance $R_p = 10\,\text{k}\Omega$, and a CNT packing density of 80%. The computed resistivity values are reported in Fig.14 for vertical vias and in Fig.15 for horizontal interconnects traces, assuming typical lengths for the local and the global levels. Due to the contact resistance, the values depend on the interconnect length: as the length increases, the effect of the contact resistance becomes more and more negligible and the resistivity of the CNT bundle outperforms that of the copper realization. This transition value is strongly dependent on the technology node and on the hierarchical level.

TABLE II: ITRS VALUES FOR ON-CHIP TRACES AND VIAS FOR 22NM AND 14 NM NODES

(ALL VALUES ARE IN NM)

TYPE		14 nm			22 nm		
		global	interm	local	global	interm	local
trace	W	105	28	14	160	44	22
	H	63	28	14	96	44	44
via	D	105	28	14	160	44	22

TABLE III: VALUES FOR THE COPPER RESISTIVITY AT ROOM TEMPERATURE [41], AS A FUNCTION OF THE INTERCONNECT WIDTH

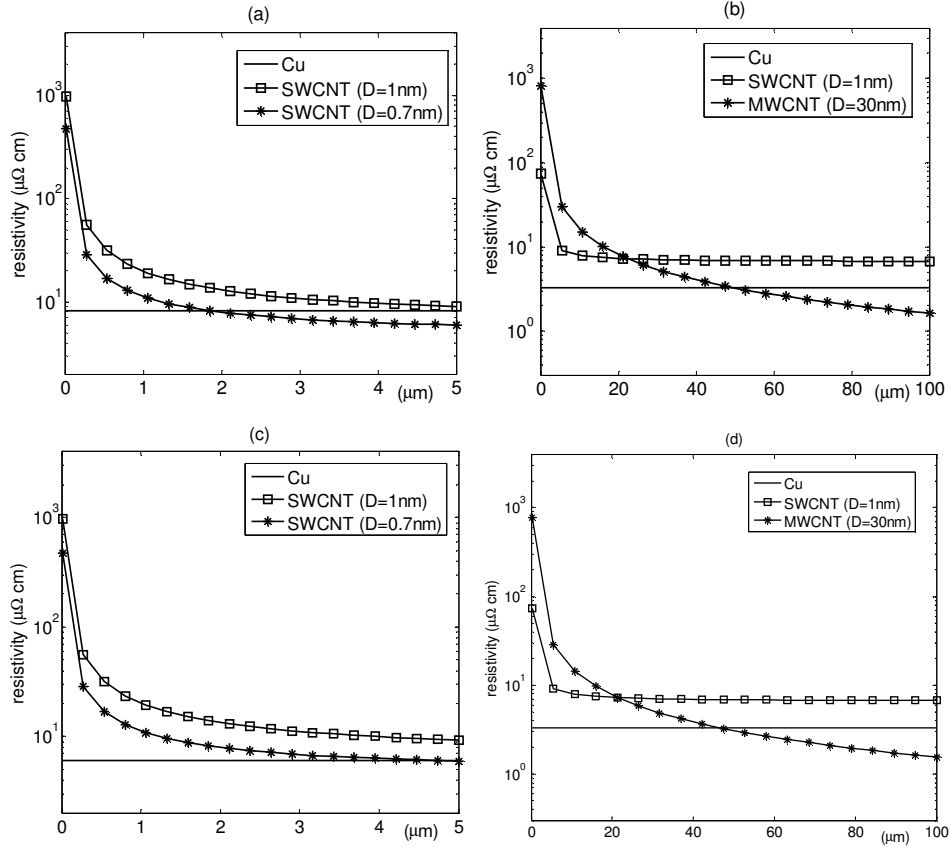| width [nm]	14	28	105	bulk
ρ [$\mu\Omega cm$]	8.19	5.39	3.29	1.72

Figure 14. Equivalent resistivity for a CNT via, made by a bundle of CNT compared to Cu via, as a function of the via height, for (a) 14-nm node, local level; (b) 14-nm node, global level; (c) 22-nm node, local level; (d) 22-nm node, global level.

Figure 15. Equivalent resistivity for a CNT trace, made by a bundle of CNT compared to Cu trace, as a function of the via height, for (a) 14-nm node, local level; (b) 14-nm node, global level; (c) 22-nm node, local level; (d) 22-nm node, global level.
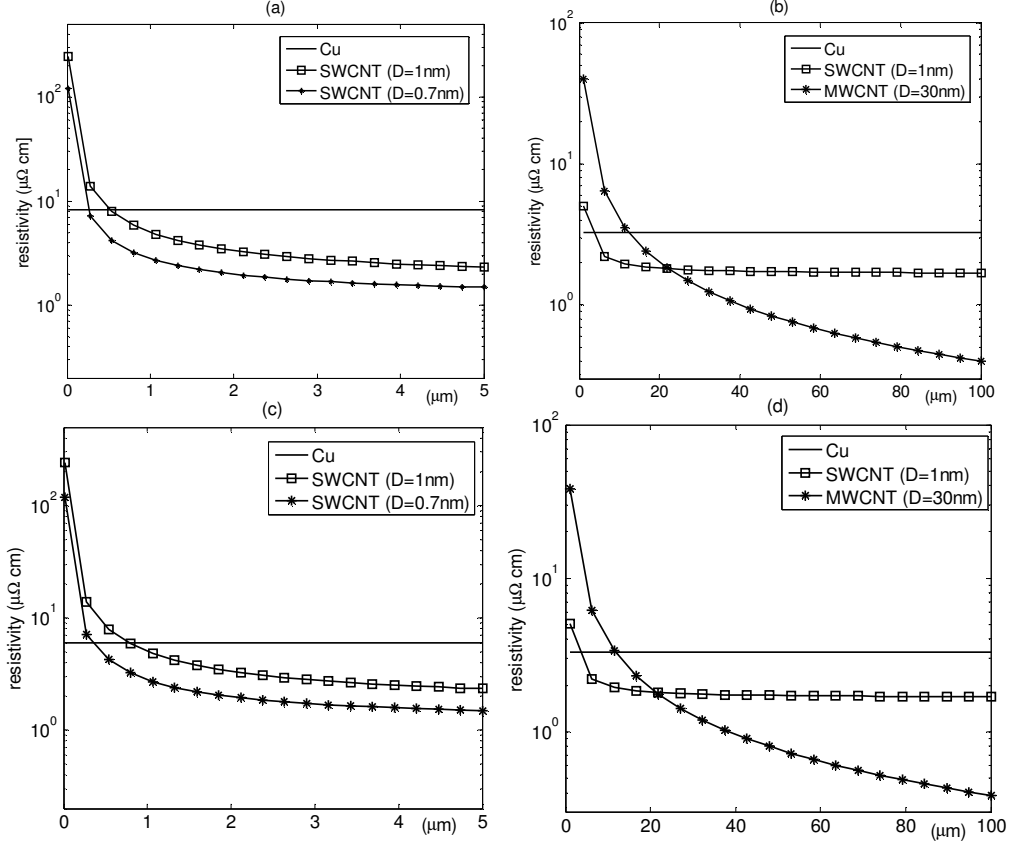
For high frequencies, also the imaginary part of resistivity plays a role, which can be put on evidence by defining the equivalent skin-depth, e.g. [12]:

$$\delta = \sqrt{\frac{2\rho_0}{\omega\mu}}\sqrt{\left[(\omega\tau)^2 + 1\right]\left(\sqrt{(\omega\tau)^2 + 1} - \omega\tau\right)}. \qquad (33)$$

Note that in classical metals the mean free path is small enough (*e.g.*, ~40nm in copper) to have $\omega\tau \ll 1$, and thus (33) provides the classical expression for δ. For CNTs, however, larger mean free path values (hundreds of μm) induce a saturation in the skin-depth as frequency increases, according to (33). In other words, a CNT bundle is much more insensitive to the skin effect as compared to a copper conductor: Figure 16 shows the computed high frequency distribution of the current density in a via, comparing the bulk copper to a MWCNT bundle solution (from [10]).
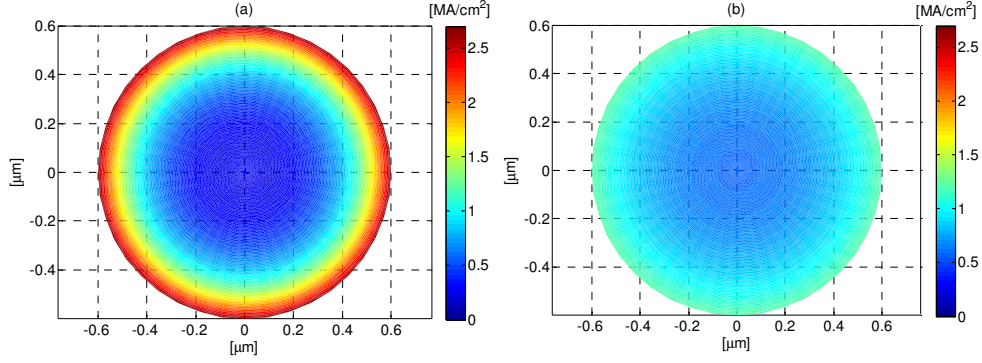
Figure 16. Distribution of the current density at 200 GHz in the cross section of a chip via made by: (a) bulk copper; (b) MWCNT bundle [10].
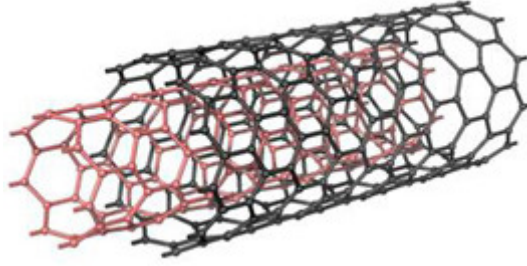

Figure 17. A double-wall carbon nanotube.

4.4.2 A bundle of CNTs in presence of intershell coupling

The model for CNT bundles presented in the previous paragraph does not take into account the possibility of a coupling between adjacent CNT shells. In order to introduce an intershell coupling effect, we can refer to the simple case of a double-wall CNT, as that depicted in Fig.17.

Introducing the intershell coupling, a generalized Ohm's law may be written to express the surface density of currents on each shell in terms of the tangential components of the electrical field on each shell [17,44]:

$$\begin{cases} \hat{J}_{z1} = \hat{\sigma}_{11}(\beta,\omega)\hat{E}_{z1} + \hat{\sigma}_{12}(\beta,\omega)\hat{E}_{z2}, \\ \hat{J}_{z2} = \hat{\sigma}_{21}(\beta,\omega)\hat{E}_{z1} + \hat{\sigma}_{22}(\beta,\omega)\hat{E}_{z1}, \end{cases} \tag{34}$$

where $\hat{\sigma}_{11} = \hat{\sigma}_{22} = \hat{\sigma}_s$ are the self conductivities given by the expressions presented in §4.3.2, whereas the mutual conductivities $\hat{\sigma}_{12} = \hat{\sigma}_{21} = \hat{\sigma}_m$ may be expressed as follows [17]:

$$\hat{\sigma}_m(\beta,\omega) \cong -i \frac{2e^2}{\pi\hbar v_F X} \frac{\omega_t \omega'}{\beta^2} \frac{1}{1 - (\beta v_F / \omega')^2} \hat{\gamma}(\beta,\omega), \qquad (35)$$

where $\omega' = \omega + i\nu$, and

$$\hat{\gamma}(\beta,\omega) = \sum_{k=1,2} \frac{\omega'}{\beta^2} \frac{2\omega_t + (-1)^k \left[1 + (\beta v_F / \omega')^2\right]}{(2\omega_t + (-1)^k \omega') - \beta^2 v_F^2}. \qquad (36)$$

In the above relations, a fundamental role is played by the tunneling frequency ω_t, related to the binding energy $\hbar\omega_t$ due to delocalization of the π-electrons for the tunnel effect. In a DWCNT we can assume that the shells are separated by the Van der Waals distance $\delta = 0.34$ nm : for such a distance, a measured value of $\hbar\omega_t \approx 35$ meV was reported, that corresponds to a tunneling frequency of $\omega_t \approx 10^{13}$ rad/s [29].

The above binding energy is fast increasing with intershell distance, and thus to include the coupling (34) in the bundle model presented in §4.3.3, we can neglect the coupling between shells which are not adjacent. In this way, matrix equation (28) modifies as follows:

$$i\omega\vec{\vec{L}}\mathbf{I} + \vec{\vec{R}}\mathbf{I} + (i\omega + \nu)\vec{\vec{L}}_{tun}\{\mathbf{I}\}+ = \mathbf{V}, \qquad (37)$$

which means that a new term adds to the inductance and resistance terms already discussed in previous paragraph. This new term is expressed as an operator acting on the spatial distribution of the current [29]:

$$\vec{\vec{L}}_{tun}\{\mathbf{I}(z,\omega)\} = \frac{1}{4\pi} \frac{\omega_t \omega'}{\omega v_F} \left(\frac{c}{v_F}\right)^2 \vec{\vec{\Theta}}\vec{\vec{L}}_M \int_{-\infty}^{+\infty} K_1(z - z'; \omega')\mathbf{I}(z',\omega)dz', \qquad (38)$$

where $\vec{\vec{\Theta}}$ is the $N_b \times N_b$ matrix defined as:

$$\mathbf{\Theta}_{ij} = \begin{cases} +1 & i = j, \\ -1 & i = j \pm 2, \\ 0 & \text{elsewhere} \end{cases} \qquad (39)$$

and the kernel is given by:

$$K_1(z;\omega') = \sin\left(\frac{2\omega_t}{v_F}|z|\right)\exp\left(-i\frac{\omega'}{v_F}|z|\right). \qquad (40)$$

In order to derive an equivalent resistivity for a CNT bundle in presence of intershell coupling, we can follow the same approach as in §4.3.3, assuming all CNT shells to be fed in parallel, hence imposing on the n-th shell the same

voltage $V_n = V_b$, where V_b is the total voltage drop along the bundle. However, the spatial dispersion introduced in (38) does not allow introducing a simple equivalent resistivity as done in (29), since the ratio between the total voltage V_b and the total current of the bundle $I_b = \sum_{n=1}^{N_b} I_n$, would no longer be independent from the distribution of the current itself. If we limit the CNT bundle length to values up to hundreds of nm, than up to the THz range the line is electrically short and it is possible to disregard the spatial variation of the current distribution. According to what shown in §4.3.3, such a length limit is fulfilled in typical on-chip interconnects, up to the global level. This condition, instead, is not satisfied where larger lengths are required, such as in Through-Silicon-Vias (TSVs) in the 3D integration or as chip-to-package interconnects [45]-[47], Assuming the above limitation, we can neglect the spatial dispersion introduced by (38) and focus on the frequency dispersion. In addition, since $\nu \approx 10^{12}$ Hz, in the THz range it is also $\omega' \approx \omega$. As a consequence, the tunneling operator (38) may be approximated as:

$$\breve{\mathbf{L}}_{tun}\{\mathbf{I}(\omega)\} \approx \frac{1}{\pi}\left(\frac{c}{v_F}\right)^2 \frac{\omega_t^2}{4\omega_t^2 - \omega^2}\breve{\mathbf{L}}_M\mathbf{I}(\omega), \tag{41}$$

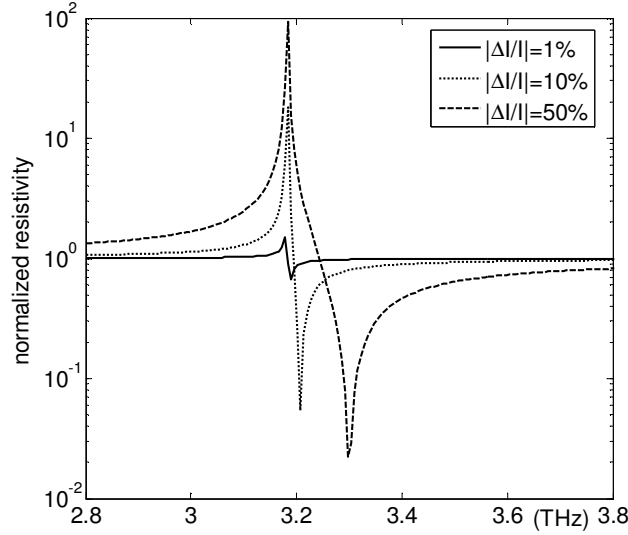and the equivalent resistivity can be again defined as in (29).

Figure 18. Absolute value of the equivalent resistivity of a double-wall CNT, carrying two different currents I_1 and I_2, for different values of the current mismatch $|\Delta I|/|I|$. The results are normalized to the resistivity for $|\Delta I| = 0$.

The effect of the coupling in the equivalent resistivity is strongly related to the distribution of the feeding currents in the bundled CNTs. The properties of matrix $\ddot{\Theta}$ (see (39)) implies that the coupling is perfectly canceled out if the currents of adjacent shells are perfectly equal, $I_n = I_s$, $n = 1..N_b$. In Fig.18 it is shown the frequency behavior of the computed equivalent resistivity for a DWCNT of outer diameter of 20 nm, assuming different levels of mismatch between the current flowing into the two shells: $|\Delta I|/|I| = |I_1 - I_2|/|I|$. It is evident how the coupling due to tunneling modifies the resistivity by introducing a resonance peak, whose amplitude and width increases as the mismatch increases.

4.5 Electrical conductivity of CNTs up to the optical range

In order to model the CNT electrical conductivity in a wider frequency range, up to the optical frequencies, a direct solution of the quantum-mechanical equations of motion for π-electrons is needed. Consider an infinitely long rectilinear single-wall CNT, oriented along the z axis and excited by the component of electromagnetic field polarized along this axis: $\mathbf{E}(\mathbf{r},t) = \mathbf{e}_z E_0 \exp(\mathbf{k} \cdot \mathbf{r})$, where $\mathbf{k}$ is the wave-vector of the exciting field, assumed to be normal to the CNT axis. In the tight-binding approximation, the motion of electrons in the CNT crystalline lattice potential is described by the Schrödinger equation, whose solution may be written in terms of Bloch wave expansion

$$\Psi(\mathbf{r},t) = \sum_q C_q(p_z,t)\Psi_q(\mathbf{p},\mathbf{r}), \tag{42}$$

where the index q stands for the collection of quantum numbers characterizing states of π-electrons with a given quasi-momentum. In the framework of the two-band model, in the following we denote the index q with either "v" or "c", which correspond to valence and conduction bands, respectively. The basis functions are the Bloch waves with amplitudes $u_q(\mathbf{r})$ periodic with respect to the arbitrary lattice vector $\mathbf{R}$ expressed as [48]:

$$\Psi_q(\mathbf{p},\mathbf{r}) = \hbar^{-1/2} \exp(i\mathbf{p} \cdot \mathbf{r}/\hbar)u_q(\mathbf{r}), \tag{43}$$

whereas the coefficients $C_q(p_z,t)$ are solutions of the equation:

$$i\hbar \frac{\partial C_q}{\partial t} = \mathrm{E}_q C_q - i\hbar e E_z^0 \frac{\partial C_q}{\partial p_z} - e E_z^0 \sum_{q'} C_{q'} R_{qq'}. \tag{44}$$

For a zig-zag CNT of chiral number m, the matrix element $R_{qq'}$ in (44) may be expressed as:

$$R_{vc}(p_z,s) = -\frac{b\gamma_0^2}{2\mathcal{E}_c^2(p_z,s)}\left[1+\cos(ap_z)\cos\left(\frac{\pi s}{m}\right)-2\cos^2\left(\frac{\pi s}{m}\right)\right], \quad (45)$$

whereas for an armchair (m,m) CNT it is:

$$R_{vc}(p_z,s) = -\frac{\sqrt{3}b\gamma_0^2}{2\mathcal{E}_c^2(p_z,s)}\sin\left(\frac{ap_z}{\sqrt{3}}\right)\sin\left(\frac{\pi s}{m}\right), \quad (46)$$

Using (45) or (46), the solution of (44) provides the surface density of the axial current, as:

$$j_z(t) = \frac{2e\gamma_0}{(\pi\hbar)^2 r_c}\sum_{s=1}^{m}\int\left\{\frac{\partial\mathcal{E}_c}{\partial p_z}\rho_{vv}+\mathcal{E}_c R_{vc}\,\text{Im}(\rho_{vc})\right\}dp_z, \quad (47)$$

where $\rho_{qq'}=C_q C_{q'}^*$ are the elements of the matrix of density. In the weak-field regime, the equations (44) can be solved in the linear approximation: if we neglect spatial dispersion, the axial conductivity in the optical range may be put in the form [48]:

$$\sigma_{zz}(\omega) = -\frac{ie^2\omega}{\pi^2\hbar r_c}\left\{\frac{1}{(\omega+i0)^2}\sum_{s=1}^{m}\int_{1stBZ}\frac{\partial F_c}{\partial p_z}\frac{\partial\mathcal{E}_c}{\partial p_z}dp_z + \right.$$
$$\left. -2\sum_{s=1}^{m}\int_{1stBZ}\mathcal{E}_c|R_{vc}|^2\frac{F_c-F_v}{\hbar^2(\omega+i0)^2-4\mathcal{E}_c^2}dp_z\right\}. \quad (48)$$

The quantities F_c, F_v are the Fermi distribution functions, obtained from (3) by substituting $\mathcal{E}\to\mathcal{E}_{c,v}-\mu_{ch}$, being μ_{ch} the electrochemical potential.

The relaxation effect can be phenomenologically incorporated in (48) by substituting $(\omega+i0)^2\to\omega(\omega+i/\tau)$. The first term on the right side of (48) describes the intraband motion of π-electrons, thus corresponding to the quasi-classical conductivity derived in Section 4.3.2, based on the Boltzmann equation. The second term on the right side of (48) describes direct transitions between the valence and the conductivity bands.

The frequency behavior of the conductivity is reported in Fig.19 for a metallic and a semiconducting zig-zag CNT. Here we assume a relaxation time of $\tau=3\,\text{ps}$ and a temperature $T_0=295\text{K}$. The contribution of free charge-

carriers to real part of the conductivity σ_{zz} is dominant at low frequencies, but is too small to be evident in both figures. The initial decay of the imaginary part of σ_{zz} with increasing frequency in Fig.19a is certainly due to free charge-carriers, but the same feature is absent from Fig.19b, because of the low density of free charge-carriers in semiconductors. As the frequency increases, $Im(\sigma_{zz})$ becomes negative. This change in sign is due to interband electronic transitions. Optical resonances appear with further increase in frequency, the frequency of the lowest resonance decreasing as the CNT radius grows. For a fixed radius, a semiconducting CNT resonates at a lower frequency than a metallic CNT.
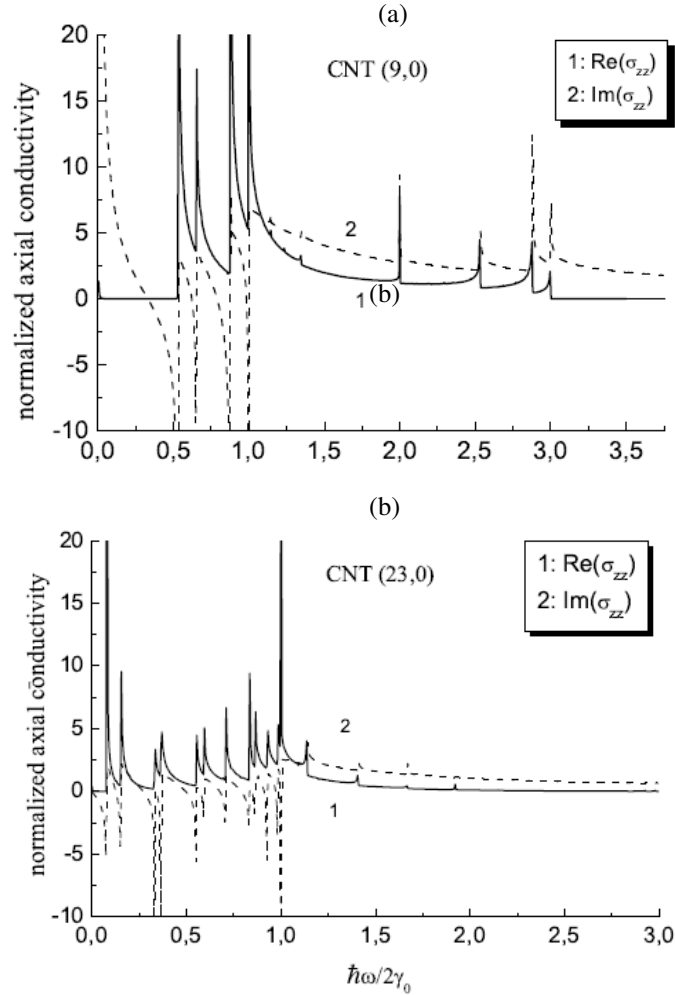

Figure 19 Frequency dependence of the total axial conductivity σ_{zz} for a zigzag CNT: (a) metallic (9;0); (b) semiconducting (23,0). The axial conductivity is normalized to $e^2/2\pi\hbar$. [18]

Conclusions

This Chapter presented the study of the electrical conductivity of CNTs, in view of their potential applications in nanoelectronics, based on fundamental physical principles.

The energy spectrum of π-electrons was calculated using the tight-binding approximation for hexagonal crystal lattice with quantum confinement in the azimuthal direction. The low-frequency model (from DC to THz) was obtained using the quasi-classical concept of 1D-Fermi electron gas. Its dynamic behavior in the electromagnetic field is described by the Boltzmann kinetic equation with a phenomenological collision term. The CNT conductivity was obtained by solving a linearized version of the above problem.

In the high-frequency range, the conductivity was modeled by means of the quantum theory of transport, based on Schrodinger equation for $\pi-$ electrons, which accounts also for interband transitions between valence and conduction zones. In the low-frequency-limit this theory goes to the quasi-classical model mentioned above. The model of MWCNT-conductivity accounts the intershell tunneling of π-electrons between neighboring sheets.

Based on the above conductivity models, transmission-line models were presented, to describe the signal propagation along single of bundled CNTs. The real values of inductance, capacitance, resistance and characteristic impedance for metallic and semiconducting CNTs were presented and discussed, in view of using CNTs as interconnects.

The theory and experimental observation of the plasmonic resonance in CNT were also described. The proposal of using CNT as a THz-nanoantenna is discussed.

References.

1. Saito R, Dresselhaus G., Dresselhaus M S 2004 Physical Properties of Carbon Nanotubes, Imperial College Press: Singapore.
2. S. Reich, C. Thomsen, and J. Maultzsch Carbon Nanotubes (Wiley-VCH, Weinheim, Germany (2004).
3. M.P. Anantram and F. Lonard, Reports on Progress in Physics, 69, 507 (2006).
4. A.S. Ilyinsky, G.Ya. Slepyan and A.Ya. Slepyan: Propagation, Scattering and Dissipation of Electromagnetic Waves, (Peter Peregrinus, London 1993).
5. G. W. Hanson, "Fundamental transmitting properties of carbon nanotube antennas," IEEE Trans. Antennas Prop., Vol. 53, pp. 3426–3435, 2005.
6. P.J. Burke, S. Li, and Z. Yu, "Quantitative theory of nanowire and nanotube antenna performance," IEEE Trans. Nanotechnol., vol. 5, pp. 314–334, Oct. 2006.
7. Slepyan G Y, Shuba M V, Maksimenko S A, and Lakhtakia A (2006) Theory of optical scattering by achiral carbon nanotubes and their potential as optical nanoantennas, Phys Rev B 73: 195416.
8. A. Maffucci, G. Miano and F. Villone, "Performance Comparison Between Metallic Carbon Nanotube and Copper Nano-interconnects," IEEE Trans. on Advanced Packaging, Vol.31, N. 4, pp. 692-699, Nov. 2008.
9. J.E. Morris Nanopackaging: Nanotechnologies and electronics packaging (Springer, New York 2008)
10. G. F. Close, S. Yasuda, B. Paul, S. Fujita and H.-S. Philip Wong, "A 1 GHz Integrated Circuit with Carbon Nanotube Interconnects and Silicon Transistors," Nano Letters, Vol.8, N. 2, pp.706-709, 2009.
11. M. V. Shuba, G. Y. Slepyan, S. A. Maksimenko, C. Thomsen, and A. Lakhtakia, "Theory of multiwall carbon nanotubes as waveguides and antennas in the infrared and the visible regimes," Phys. Rev. B, vol. 79, no. 15, pp. 155403–155403, 2009.
12. H. Li, C. Xu, N. Srivastava, and K. Banerjee, "Carbon Nanomaterials for Next-Generation Interconnects and Passives: Physics, Status, and Prospects," IEEE Trans. on Electron Devices, Vol.56, n.9, pp.1799-1821, 2009.
13. L. Ding, S. Liang, T. Pei, Z. Zhang, S. Wang, W. Zhou, J. Liu, L-M. Peng, "Carbon nanotube based ultra-low voltage integrated circuits: Scaling down to 0.4 V," Applied Physics Letters, vol. 100, n.26, pp.263116 - 263116-5, 2012.
14. A. G. Chiariello, A. Maffucci, G. Miano, "Circuit Models of Carbon-based Interconnects for Nanopackaging, IEEE Transactions on Components, Packaging and Manufacturing, Vol.3, No.11, pp.1926-1937, Nov. 2013.
15. I. Valitova, M. Amato, F. Mahvash, G. Cantele, A. Maffucci, C. Santato, R. Martel, and F.Cicoira, "Carbon nanotube electrodes in organic transistors", Nanoscale, Vol.5, 2013, pp.4638-4646.
16. R. R. Hartmann, J. Kono, and M. E. Portnoi,"Terahertz science and technology of carbon nanomaterials," Nanotechnology, vol. 25, 322001, July 2014.
17. Miano, G.; Forestiere, C.; Maffucci, A.; Maksimenko, S.A. and Slepyan, G.Y. Signal propagation in single wall carbon nanotubes of arbitrary chirality, IEEE Transactions on Nanotechnology, 2011, 10, 135-149.
18. G.Ya. Slepyan, S.A. Maksimenko, A. Lakhtakia, O. Yevtushenko, and A.V. Gusakov, "Electrodynamics of carbon nanotubes: Dynamic conductivity, impedance boundary conditions, and surface wave propagation," Phys. Rev. B, vol. 60, pp. 17136–17149, Dec. 1999.
19. F. G. Bass and A. A. Bulgakov, Kinetic and Electrodynamic Phenomena in Classical and Quantum Semiconductor Superlattices (Nova, New York, 1997).

20. Y. Miyamoto, S.G. Louie and M.L. Cohen, "Chiral Conductivities of Nanotubes," Phys. Rev.Lett. 76, 2121 (1996).
21. O. M. Yevtushenko, G. Ya. Slepyan, S. A. Maksimenko, A. Lakhtakia, and D. A. Romanov, "Nonlinear electron transport effects in a chiral carbon nanotube," Phys. Rev. Lett. 79, 1102-1105 (1997).
22. G.Ya.Slepyan, S.A.Maksimenko, A.Lakhtakia, O.M.Yevtushenko, and A.V.Gusakov, Electronic and electromagnetic properties of nanotubes. Phys. Rev. B 57, 9485-9497 (1998).
23. C. Forestiere, A. Maffucci, G. Miano, "On the Evaluation of the Number of Conducting Channels in Multiwall Carbon Nanotubes," IEEE Transactions on Nanotechnology, Vol.10, No.6, 1221-1223, 2011.
24. M. Lundstrom, Fundamentals of carrier transport (Cambridge Univ. Press, Cambridge, U.K., 2000).
25. E. Pop, D. A. Mann, K. E. Goodson, and H. J. Dai, "Electrical and thermal transport in metallic single-wall carbon nanotubes on insulating substrates," *J. Appl. Phys.*, vol. 101, no. 9, pp.093710, May 2007.
26. Slepyan G Y, Shuba M V, Maksimenko S A, Thomsen C, and Lakhtakia A (2010) Terahertz conductivity peak in composite materials containing carbon nanotubes: Theory and interpretation of experiment, Phys Rev B, 81: 205423.
27. Shuba M V, Paddubskaya A G, Plyushch A O, Kuzhir P P, Slepyan G Y, Maksimenko S A, Ksenevich V K, Buka P, Seliuta D, Kasalynas I, Macutkevic J, Valusis G, Thomsen C, and Lakhtakia A (2012) Experimental evidence of localized plasmon resonance in composite materials containing single-wall carbon nanotubes, Phys Rev B 85: 165435.
28. F. Bommeli, L. Degiorgi, P. Wachter, W.S. Bacsa, W.A. De Heer, L. Forro, "Evidence of anisotropic metallic behaviour in the optical properties of carbon nanotubes", Solid State Comm. vol. 99, pp. 513-517, (1996).
29. A. Ugawa, A.G. Rinzler, "Far-infrared gaps in single-wall carbon nanotubes," Phys. Rev. B 60, R11605 (1999).
30. M. E. Itkis, S. Niyogi, M. E. Meng, M. A. Hamon, H. Hu, and R.C. Haddon, "Spectroscopic study of the Fermi level electronic structure of single-walled carbon nanotubes," Nano Lett. 2, 155–159 (2002).
31. F. L. Shyu and M. F. Lin, "Electronic and Optical Properties of Narrow-Gap Carbon Nanotubes," J. Phys. Soc. Jpn. 71, 1820-1823, 2002.
32. T.-I. Jeon, K.-J. Kim, C. Kang, S.-J. Oh, J.-H. Son, K. H. An, D.J. Bae, and Y. H. Lee, "Terahertz conductivity of anisotropic single walled carbon nanotube films"Appl. Phys. Lett. 80, 3403 (2002).
33. F. Borondics and K. Kamaras, M. Nikolou, D. B. Tanner, Z. H. Chen, and A. G. Rinzler, "Charge dynamics in transparent single-walled carbon nanotube films from optical transmission measurements," Phys. Rev. B 74, 045431 (2006).
34. T. Kampfrath, K. von Volkmann, C. M. Aguirre, P. Desjardins, R. Martel, M. Krenz, C. Frischkorn, M. Wolf, and L. Perfetti, Mechanism of the far-infrared absorption of carbon-nanotube films, Phys. Rev. Lett. 101, 267403 (2008).
35. N. Akima, Y. Iwasa, S. Brown, A. M. Barbour, J. Cao, J. L. Musfeldt, H. Matsui, N. Toyota, M. Shiraishi, H. Shimoda, and O. Zhou, "Strong anisotropy in the far-infrared absorption spectra of stretch-aligned,single-walled carbon nanotubes,"Adv. Mater. 18, 1166 –1169 (2006).
36. Shuba M V, Paddubskaya A G, Kuzhir P P, Maksimenko S A, Ksenevich V K, Niaura G, Seliuta D, Kasalynas I, Valusis G (2012) Soft cutting of single-wall carbon nanotubes by low temperature ultrasonicatin in a mixture of sulfuric and nitric acids, Nanotechnology 23: 495714.
37. Zhang Q, Hároz E H, Jin Z, Ren L, Wang X, Arvidson R S, Lüttge A, and Kono J (2013) Plasmonic nature of the terahertz conductivity peak in single-wall carbon nanotubes, Nano Lett 13: 5991- 5996.

38. A. M. Nemilentsau, M. V. Shuba, G. Ya. Slepyan, P. P. Kuzhir, S. A. Maksimenko, P. N. D'yachkov, A. Lakhtakia, Substitutional doping of carbon nanotubes to control their electromagnetic characteristics, Phys. Rev. B 82, 235424 (2010).

39. M. V. Shuba, A. G. Paddubskaya, P. P. Kuzhir, G. Ya. Slepyan, D. Seliuta, I. Kašalynas, G. Valušis, A. Lakhtakia, Effects of inclusion dimensions and p-type doping in the terahertz spectra of composite materials containing bundles of single-wall carbon nanotubes J. Nanophoton. 6, 061707 (2012).

40. T. Morimoto, S.-K. Joung, T. Saito, D. N. Futaba, K. Hata, and T. Okazaki, "Length-dependent plasmon resonance in single-walled carbon nanotubes," ACS Nano, vol. 8, pp. 9897-9904 (2014).

41. ITRS, International Technology Roadmap for Semiconductors, http://public.itrs.net, (Ed. 2013).

42. W. Steinhögl et al., "Comprehensive study of the resistivity of copper wires with lateral dimensions of 100 nm and smaller," Journal of Applied Physics, Vol.97, p.023706, 2005.

43. C. Stanciu, R.Ehlich, V. Petrov, O. Steinkellner, J. Herrmann, I.V. Hertel, G. Ya. Slepyan, A. A. Khrutchinski, S.A. Maksimenko, F. Rotermund, E.E.B. Campbell, and F. Rohmund, Experimental and theoretical study of third-order harmonic generation in carbon nanotubes. Appl. Phys. Lett. 81 (21), 4064-4066 (2002).

44. M. V. Shuba, G. Y. Slepyan, S. A. Maksimenko, C. Thomsen, and A. Lakhtakia, "Theory of multiwall carbon nanotubes as waveguides and antennas in the infrared and the visible regimes," Phys. Rev. B, vol. 79, no. 15, pp. 155403–155403, 2009.

45. A. Naeemi and J. D. Meindl, "Performance Modeling for Single- and Multiwall Carbon Nanotubes as Signal and Power Interconnects in Gigascale Systems," *IEEE Trans. on Electron Devices*, Vol. 55, N.10, pp. 2574-2582, Oct. 2008.

46. A. G. Chiariello, A. Maffucci and G. Miano, "Electrical Modeling of Carbon Nanotube Vias," *IEEE Trans. on Electromagnetic Compatibility,* Vol.54, no.1, pp. 158-166, Feb.2012.

47. T. Wang, S. Chen, D. Jiang, Y. Fu, K. Jeppson, L. Ye, and J. Liu, "Through-Silicon Vias Filled with Densified and Transferred Carbon Nanotube Forests," *IEEE Electr. Device Letters*, vol.33, no.3, pp.420 – 422, 2012.

48. S.A. Maksimenko and G.Ya. Slepyan: Electrodynamics of carbon nanotubes. J. Commun. Technol. Electron. 47, 235-252 (2002).